Available online at www.sciencedirect.com
SCIENCE DIRECT®
Journal of Nuclear Materials 326 (2004) 163–174
journal of nuclear materials
www.elsevier.com/locate/jnucmat

Ternary Zr–Nb–Fe(O) system: phase diagram at 853 K and corrosion behaviour in the domain Nb < 0.8%

P. Barberis [a,*], D. Charquet [a], V. Rebeyrolle [b]

[a] CEZUS Research Centre, Avenue Paul Girod, F-73403 Ugine cedex, France
[b] FRAMATOME-ANP, 10 rue Juliette Récamier, 69456 Lyon cedex 06, France

Received 23 April 2003; accepted 8 January 2004

Abstract

Several zirconium-based alloys in the domain Nb < 0.8 wt%, Fe < 0.5 wt% and Sn < 1 wt% (and oxygen in the range 600–1200 ppm) were elaborated. Several process routes were used to produce sheets and claddings. The microstructure was investigated by TEM, with a particular attention payed to the SPP nature and composition. Corrosion tests in steam in autoclave or in air were performed. This study allowed us to precise the isothermal cut at 853 K of the Zr-rich corner of the Zr–Nb–Fe ternary phase diagram, and particularly the solubility limit of Nb in αZr which appears equal to 0.37 ± 0.05 wt%, which is much lower than the usually assumed value of 0.6 wt%. In the investigated range, the tin content has no significant influence on the phase diagram, but tin degrades the corrosion resistance in autoclave at 773 and 688 K. Last, the steam corrosion behaviour shows a very strong dependence on the exact process for the lowest SPP-VF, and very high weight gain can be obtained. The air oxidation is much less affected by this parameter.

PACS: 81.30.Bx; 81.65.Mn

1. Introduction

A lot of work has been devoted through the recent years to the ternary Zr–Nb–Fe system [1–5], possibly with some tin or oxygen additions, due to the fact that the Nb containing alloys have supplanted the old Zircaloy-4 in the PWRs. Indeed, the M5™ alloy [6–8] is mainly a Zr1Nb-O alloy, while E635 [9–11] and ZIRLO™ [12–17] contain in addition Fe and Sn. As firmly established in the past 20 years, the microstructure of the alloys, which evolves under irradiation, acts on the corrosion behaviour and mechanical properties, as well as on the irradiation growth of the nuclear fuel components. It is thus very important to accurately control the microstructure, and to relate it to these properties.

The ternary ZrNbFe phase diagram has been investigated in the low temperature domain (about 843–1023 K) [1,2] or in the high temperatures (about 1023–1273 K) [3,4]. It has been shown that tin, at least up to 1.3 wt% does not influence the ternary phase diagram Zr–Nb–Fe in a significant way [2]. The existence of two ternary intermetallic compounds, the hexagonal $Zr(Nb,Fe)_2$ and the cubic $(Zr,Nb)_4Fe_2$ and their composition have been determined, but their detailed crystallographic structure is not accurately known [1,2]. However in these studies, the lower Nb contents have not been investigated in details, and specifically, the Nb solubility limit as a function of Fe content is not well known. In the literature, the solubility limit of Nb in the Zr–Nb diagram is set to about 0.6 wt% from an old study [18].

A recent paper investigated the low Nb binary alloys (Nb ranging from 0.1 to 3 wt%, and containing 420 ppm

* Corresponding author. Tel.: +33-4 7989 3068; fax: +33-4 7989 3500.
E-mail address: pierre.barberis@framatome-anp.com (P. Barberis).

0022-3115/$ - see front matter © 2004 Elsevier B.V. All rights reserved.
doi:10.1016/j.jnucmat.2004.01.007

iron) from microstructure and corrosion point of view [5]. For niobium contents ranging from 0.3 to 3.0 wt%, after heat treatment at 843 K (below the temperature of the eutectoid decomposition of βZr (19% Nb) into αZr and βNb, that is of 873 ± 5 K [2]), they found Fe- and Nb-containing second phase particles (SPP), and deduced that the niobium content in the αZr matrix was lower than 0.3 wt% in the presence of iron. However, they worked on β-quenched and annealed structures, and we can wonder if, despite long annealing times, the microstructure is really representative of cladding or structural materials [5]: the absence of further hot and cold deformation followed by heat treatments well below the beta phase prevents the formation of equiaxed grains, which are typical of (recrystallised) cladding.

The corrosion behaviours of ternary ZrNbFe alloys is also particularly interesting: in binary ZrNb alloys, the corrosion mechanism has been evidenced to be different from the 'classical' Zircaloy corrosion [19–21]: either due to βNb or to Nb in solid solution, it could involve an interface controlling step. For Zircaloy, it is generally thought that the controlling step is rather diffusion of oxygen ions through a dense layer, whose thickness can vary, though the second phase particles have been shown to play a great role [22] and recent experiments show that in some particular oxidation conditions other mechanism could prevail [23]. The ternary ZrNbFe alloys, contain both niobium in solid solution in the αZr matrix, like binary ZrNb alloys, and depending on the composition, intermetallics SPPs which could act in a similar way to Zircaloy SPPs. It has been proposed recently that the Nb content in solid solution would be prevalent compared to SPPs [5].

In order to have a more detailed picture of the low-Nb part of the Zr–Nb–Fe phase diagram, we investigated several alloys in the region Nb < 0.8%, Fe < 0.5%, Sn < 1%. In addition, the corrosion behaviour being an important aspect of the alloy properties, we intended to assess their corrosion behaviour in several test conditions.

2. Materials and experiments

2.1. Materials

Three sets of materials differing by their composition and process routes were elaborated at a laboratory scale, both sheets and cladding tubes. Their chemical composition is given in Table 1. It was determined by inductive coupled plasma optical emission spectroscopy (ICP-OES) for Nb, Sn, Fe and Cr and by LECO melting and infrared detection for O.

The sheets 1–4 contain no tin and low iron; the sheets 5–9 and 10–14 exhibit increasing niobium content (from 0.3 to 0.7 wt%), low iron content, and differ mainly by their tin content (respectively 0.5 and 1 wt%). Finally the sheets 15–17 were elaborated to investigate the high iron (0.45 wt%) region.

Cladding tubes were processed from an ingot with niobium gradient along the axis (it does not induce any gradient for the other elements). The niobium content ranged from 0.05 to 0.56 wt% and the iron content was set at 300 wt ppm.

Sheets were obtained from 1.5 kg ingots melted 3 times in a pseudo-levitation furnace, then transformed

Table 1
Chemical composition of the alloys (determined on sheets and cladding by ICP-OES for Nb, Sn, Fe and Cr and by LECO instrumentation for O)

Mark	Nb (wt%)	Sn (wt%)	Fe (wt ppm)	Cr (wt ppm)	O (wt ppm)	Process (see Table 2)
1	0.41	0	399	21	630	#1
2	0.41	0	175	25	840	#1
3	0.50	0	166	25	670	#1
4	0.62	0	161	22	610	#1
5	0.29	0.48	100	20	650	#2
6	0.39	0.49	100	21	870	#2
7	0.47	0.47	100	19	640	#2
8	0.60	0.49	100	21	630	#2
9	0.65	0.48	100	21	640	#2
10	0.29	1.00	70	20	650	#2
11	0.38	1.01	70	19	670	#2
12	0.48	0.96	70	20	660	#2
13	0.54	1.00	60	21	650	#2
14	0.68	0.99	60	19	650	#2
15	0.36	0	4200	19	640	#2
16	0.46	0	4300	21	710	#2
17	0.82	0	4500	20	590	#2
Cladding	0.05–0.56	0	300	45	1200	

Table 2
Process routes

Sheets-process #1	Sheets-process #2	Cladding
Pseudo-levitation induction melting	Pseudo-levitation induction melting	VAR melting
Water quenching	Air cooling	Water quenching
Hot rolling 1063 K	Hot rolling 853 K	Extrusion
Annealing 853 K	Annealing 853 K	
Several cycles of cold rolling and annealing at 853 K (total time in temperature: 14 h)	Several cycles of cold rolling and annealing at 853 K (total time in temperature: 12 h)	Several cycles of pilgering and annealing at 853 K (total time in temperature: 8 h)
Final thickness 0.4 mm	Final thickness 1.5 mm	Cladding thickness 0.57 mm

using a usual sequence of quenching, hot rolling, and several cycles of cold rolling and low temperature (853 K) anneal down to the final thickness of 0.4 or 1.5 mm. Their composition was designed to investigate mainly the effect of niobium in the low range (0.3–0.8 wt%), but also the effect of tin (0–1 wt%), and of iron (60–4500 wt ppm).

The main characteristics of the processes are summarised in Table 2.

2.2. Experiments

The experiments and experimental devices are very classical: optical microscopy both in bright field and polarised light, TEM and corrosion in autoclave or in furnace.

TEM was performed on thin foils to determine the nature of SPP (through SAD), while their composition was obtained on extractive replicas. A JEOL TEM operated at 200 KV with a standard tungsten gun was used; composition was obtained through a EDX system. About 10 SPP of each types were analysed for composition in each sample; the results given below are the mean over these 10 measurements.

Corrosion was performed in autoclave under 10.5 MPa steam at 773 and 688 K. Some samples were tested in autoclave at 688 K under static low pressure steam (0.1 MPa, that is atmospheric pressure), or in air at 688 K in an open furnace, by analogy with the work performed on binary alloys [22].The sheet samples were pickled in a standard HF/HNO3/water bath before the corrosion test, while the cladding were tested in the as-received surface state.

3. Results

3.1. Microstructure (optical microscopy)

In all the cases, the microstructure is recrystallised with equiaxed grains. The general trend is that increasing the Nb and Fe content decreases the grain size. Fig. 1 illustrates this behaviour. It seems coherent with a control of the grain size by the SPP size and volume fraction due to the interaction of the grain boundary with the SPPs, as proposed in binary alloys [22].

In bright field in optical microscopy, the SPPs appear more numerous for higher niobium and iron content, and are uniformly distributed for cladding. For sheets, some alignments remain, due to the lower deformation after the quench.

3.2. SPP nature and SPP size

The main phases encountered in the investigated materials are, in addition to the αZr matrix, βNb, the hexagonal $Zr(Nb,Fe)_2$ and the cubic $(Zr,Nb)_4Fe_2$. Their crystallography is given in Table 3. The hexagonal $Zr(Nb,Fe)_2$ can contain some Cr remaining as an impurity in the alloy, even for content as low as 20 wt-ppm and should then be written $Zr(Nb,Fe,Cr)_2$. We will as a first approximation and to avoid excessive complexity add the chromium content to the iron content.

Some Zr_2Fe SPP were found, and their occurrence is discussed later (Section 4.1).

A few cubic βZr containing about 19 wt% Nb and possibly very low amounts of Fe (<2%) were found occasionally (in the sheets), as well as rare Si-containing particles (though the Si content was about or lower than 10 wt ppm).

The nature of SPPs (determined by SAD in TEM) observed in the alloys is given in Table 4.

The following results appear:

- The tin content (in the range 0–1 wt%) does not influence the presence of phase; thus the presence of SPP depends exclusively on the niobium and iron content.
- When decreasing the niobium content and/or raising the iron content, we are going through several phase domains: a binary domain αZr + βNb (not investigated in this study), then a ternary αZr + βNb + $Zr(Nb,Fe)_2$, then a binary αZr + $Zr(Nb,Fe)_2$, another ternary αZr + $Zr(Nb,Fe)_2$ + $(Zr,Nb)_4Fe_2$. For very low Nb and high Fe contents, there should be a ternary

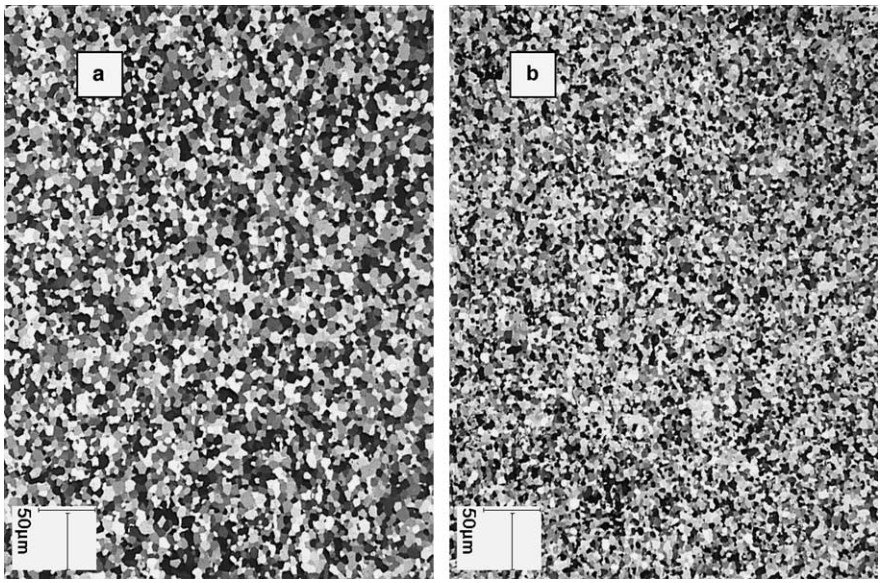

Fig. 1. Optical microscopy in polarised light on two claddings: (a) 0.07 wt% Nb and (b) 0.56 wt% Nb.

Table 3
Crystallography of the main phases found in the investigated alloys

	Symmetry	Space group	Number of atoms per unit cell	a (nm)	c (nm)	Cell volume (nm3)	Density (g/cm^3)
αZr	Hexagonal		1×6	0.3231	0.5148	0.14	6.51
βNb	Cubic		1×2	0.33		0.036	8.59
$Zr(Nb,Fe)_2$	Hexagonal	$P6_3/mmc$	3×12	0.5366	0.8792	0.658	7.5
$(Zr,Nb)_4Fe_2$	Cubic	Fm-3m or F-43m	6×16	1.215		1.794	7.1
$Zr(Fe,Cr)_2$	Hexagonal	$P6_3/mmc$	3×12	0.505	0.825	0.558	7.12
$Zr(Fe,Cr)_2$	Cubic	Fd-3m	4×3	0.72		0.373	6.98
Zr_2Fe	Tetragonal	I4/mcm	4×3	0.6385	0.5596	0.228	6.94

The data for $Zr(Nb,Fe)_2$ and $(Zr,Nb)_4Fe_2$ have been taken from [1], except for the density and atoms per unit cell.

αZr + $(Zr,Nb)_4Fe_2$ + Zr_3Fe domain, but as no Zr_3Fe was found in this study, the picture is still unclear, and we cannot know the limit for appearance and stability of Zr_3Fe. A tentative phase diagram will be proposed below.

- In some cases, Zr_2Fe SPPs, possibly containing small niobium amounts are found, generally when the cubic $(Zr,Nb)_4Fe_2$ are expected.
- For the two lowest Nb content in the cladding, that is 0.05 and 0.17 wt%, two types of $Zr(Nb,Fe)_2$ were found: the classical one with the hexagonal structure, and another one with the cubic structure (cell parameter $a = 0.72$ nm determined from SAD). This structure could be related to the C15 $Zr(Fe,Cr)_2$ phase observed in the ZrFeCr ternary diagram for high Fe or Cr contents.

As a rough estimation, the size depends only on the SPP type. It is about 60 nm for βNb, 120 nm for hexagonal $Zr(Nb,Fe)_2$ and 300 nm for cubic $(Zr,Nb)_4Fe_2$.

3.3. SPP composition

The SPP composition is given in Table 4. An extensive discussion of their evolution will be found in Section 4.

No tin containing SPP was detected, whatever the alloy. The tin content does not seem to affect the SPP composition as can be deduced from the comparison of the two sets of sheets with process #2, respectively marks 5–9 and 10–14. This fact was already known [2].

The βNb SPP contains between 85 and 91 at.% Nb and no detectable amount of iron. It is probable that the

Table 4
SPP nature and composition (in at.%, in the order Zr–Nb for βNb, Zr–Nb–Fe-Cr for the hexagonal $Zr(Nb,Fe,Cr)_2$ and Zr–Nb–Fe for the cubic $(Zr,Nb)_4Fe_2$) determined by TEM

Mark	Alloy composition		SPP nature and composition			
	Nb (wt%)	Fe (wt ppm)	βNb	$Zr(Nb,Fe,Cr)_2$	$(Zr,Nb)_4Fe_2$	Remarks
1	0.41	399	9.52–90.5	36.2–35.3–26.4–2.1	62.0–12.2–26.6	Few βNb
2	0.41	175	8.7–91.3	35.9–39.2–21.9–3.0		
3	0.50	166	10.5–89.5	36.5–39.8–20.3–3.5		
4	0.62	161	10.0–90.0	36.0–40.0–19.9–4.1		
5	0.29	100		36.2–30.9–26.1–6.7		
6	0.39	100	12.3–87.7	37.1–36.3–21.6–5.1		
7	0.47	100	14.1–85.9	35.7–35.4–23.1–5.8		
8	0.60	100	13.8–86.2	35.6–37.9–22.1–4.5		Few βZr
9	0.65	100	14.7–85.3	35.3–39.8–21.0–3.9		Few βZr
10	0.29	70		38.8–27.8–27.0–6.5		Few Zr_2Fe
11	0.38	70	12.7–87.3	36.2–33.8–24.2–5.8		Few Zr_2Fe
12	0.48	70	15.6–84.6	36.8–37.0–22.0–4.2		
13	0.54	60	13.9–86.1	36.0–36.1–22.4–5.5		
14	0.68	60	13.5–86.5	36.5–37.5–21.1–4.9		
15	0.36	4200		35.6–33.8–30.6	60.6–7.6–31.8	
16	0.46	4300		36.4–32.1–31.5	60.3–9–30.7	
17	0.82	4500		36.4–34.2–29.4	57.4–11.4–31.2	
Cladding	0.05	300		36.3–4.4–43.0–16.3[a]	Zr_2Fe: 74.6–1–24.4	
Cladding	0.17	300		37.5–18.1–32.8–11.6[a]	67.3–5.3–27.4	Few Zr_2Fe
Cladding	0.20	300		34.9–19.0–35.9–10.2	65.8–6–28.1	Few Zr_2Fe
Cladding	0.22	300		34.9–20.0–34.20–9.4	66.8–6.2–26.9	Few Zr_2Fe
Cladding	0.27	300		36.9–24.2–30.9–8.0	62.8–9–28.2	Few Zr_2Fe
Cladding	0.37	300		35.8–31.5–26.5–6.2		Few Zr_2Fe
Cladding	0.55	300	10.8–89.2	35.6–36.3–24.1–4.0		

[a] These SPPs are found in the classical hexagonal structure and in a cubic form.

higher the Nb content, the closer from equilibrium. The lowest contents are found on sheets obtained through the process #2.

In the hexagonal $Zr(Nb,Fe)_2$, the zirconium content is rather stable around 36 ± 1 at.%, value slightly higher than the stoichiometric value. On the contrary, the Nb content varies in a significant way depending on the niobium and iron content of the alloy from 40 at.% down to 20 or even 4 at.% for the lowest Nb and Fe content in the cladding (Fig. 2). It may be noted in addition that above 0.4–0.5 wt% Nb in the alloy, the at.% Nb in $Zr(Nb,Fe)_2$ remains roughly stable upon increasing Nb content. It should however be reminded that in the very low Nb and Fe alloys, this SPP is found in both hexagonal and cubic structures, which could not be distinguished from analytical point of view.

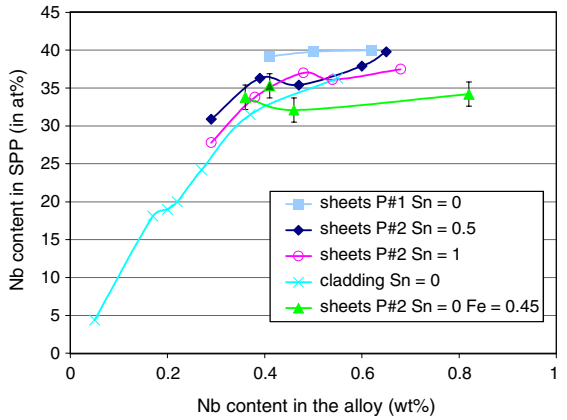

Fig. 2. Nb content in the hexagonal $Zr(Fe,Nb)_2$ SPP versus the Nb content in the alloy.

For the cubic $(Zr,Nb)_4Fe_2$, the iron content seems rather constant at around 28 or 30 at.% (depending slightly on the sample set: sheets or cladding), while the Nb contents increases (for a given process) with the Nb content of the alloy, as stated previously for the $Zr(Fe,Nb)_2$ SPPs. The Zr_2Fe SPP seems to admit low Nb content (about 1 at.% or less, which is the detection limit of the technique), and could be considered as the 'low end' of the cubic SPP when decreasing the niobium content.

To further interpret the data, we will consider both the thermodynamic aspect (equilibrium and phase diagram), and the kinetics.

3.4. Corrosion results: 688 and 773 K in autoclave, 688 K in air and low pressure steam

Corrosion results are presented below.

3.4.1. Corrosion in autoclave at 773 K under 10.5 MPa steam

The 773 K steam corrosion test in autoclave was performed for up to 28 days. The results after 24 h, presented in Fig. 3 as a function of the Nb content, show clearly that very high weight gains are obtained for low Nb contents, followed by a sharp drop and a plateau for Nb contents greater than 0.4–0.6 wt%. The appearance of the oxide layer evolves concomitantly: for the lowest Nb contents (Nb < 0.25 wt%), it is a white uniform corrosion layer; for intermediate Nb contents, nodules can be distinguished over a thin black uniform oxide layer, whose number decreases with increasing Nb content. On the plateau, a shiny black uniform oxide layer is exclusively seen. The tin content do have an impact on corrosion: for the sheets with P#2 process, the weight gain increases when going from 0.5% to 1.0% Sn. The same tendency holds when comparing the cladding which do not contain tin to the sheets with P#2 process, though the comparison is not strictly valid since the sample geometry and the process are different. However, the influence of tin is much lower than the influence of niobium in the investigated range.

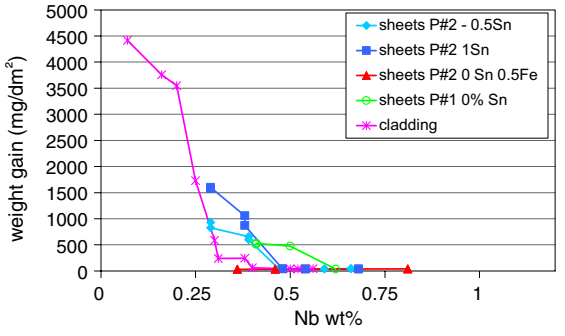

Fig. 3. Corrosion results on the various materials versus the Nb content after a 773 K 10.5 MPa 24 h steam corrosion test in autoclave.

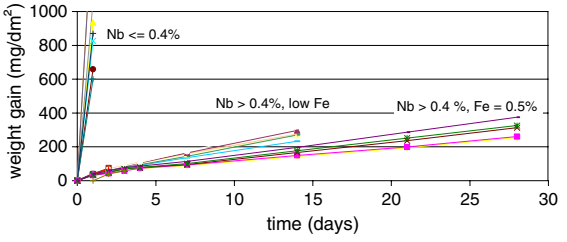

Fig. 4. Corrosion kinetics at 773 K in 10.5 MPa steam in autoclave, for the sheets process #2.

Corrosion kinetics at 773 K were established for the sheets process #2, and are presented in Fig. 4. We can see that for high enough niobium (and iron) content, the kinetics is parabolic at the beginning, followed by a more or less linear step, but there is a continuous transition (no acceleration) between the two steps. In addition, high iron (and lower tin) content leads to lower weight gains.

3.4.2. Corrosion in autoclave at 688 K under 10.5 MPa steam

The corrosion behaviour at 688 K under 10.5 MPa steam in autoclave was investigated for long duration. We found as previously very high weight gain for low Nb contents, followed by a sharp drop and a plateau. As previously, we can see that on samples from sheet P#2, the concomitant reduction of tin and increase of iron decrease the weight gain; on sample from sheet P#1, the comparison between the samples mark 1 and 2 show the benefit of increased iron content (Fig. 5).

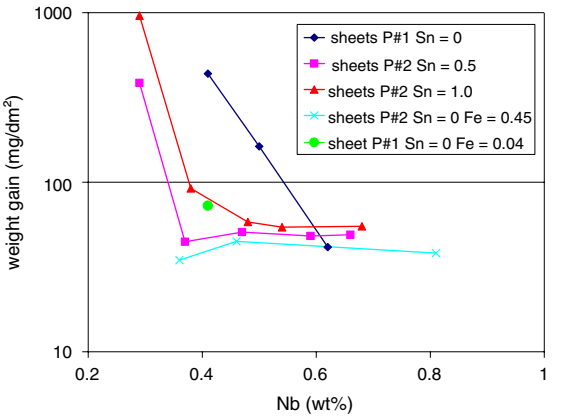

Fig. 5. Corrosion results on the sheets versus the Nb content after a 688 K 10.5 MPa steam corrosion test in autoclave after 28 days.

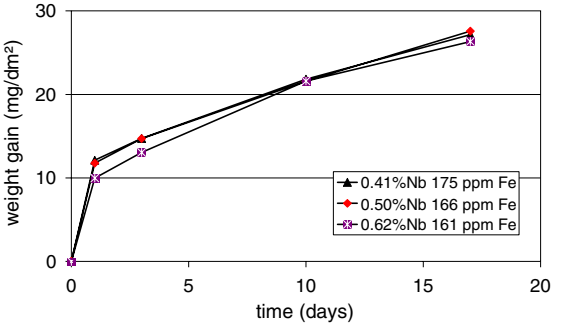

Fig. 6. Corrosion kinetics of sheets P#1 under 0.1 MPa steam.

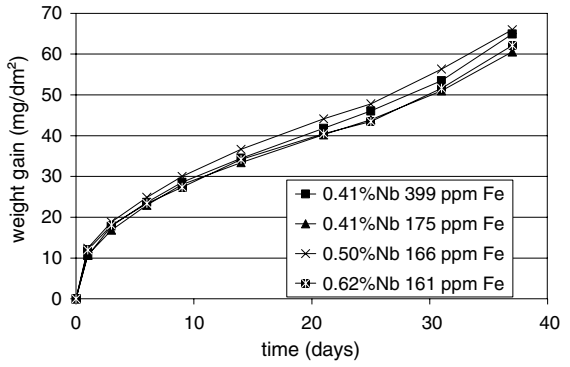

Fig. 7. Corrosion kinetics of sheets P#1 under 0.1 MPa air.

3.4.3. Low pressure test in steam or in air at 688 K

We performed low pressure tests only on the sheets P#1.

Under 0.1 MPa steam, the kinetics is of parabolic type up to 17 days; the niobium in the range explored (0.41–0.62 wt%) does not seem to have an influence (Fig. 6).

Under 0.1 MPa air, the kinetics shows a transition between a first parabolic-type kinetics and another one presenting an acceleration at the transition (Fig. 7). No significant effect of niobium or iron can be detected. Rather surprisingly, the kinetics is higher in air than in steam.

4. Discussion

We will now discuss the previous results, first from a microstructural point of view, proposing an isothermal cut at 853 K of the phase diagram, and then from a corrosion point of view, trying to understand what are the main factors acting upon the corrosion.

4.1. Evolution of phases with Nb and Fe content of the alloy

For all investigated alloys, we found Nb-bearing SPP (either hexagonal or cubic intermetallics, in some cases Zr_2Fe or $Zr(Fe,Cr,Nb)_2$, or βNb or βZr) besides the αZr matrix. All these phases are known in the zirconium alloys; in the ternary ZrNbFe system they were expected, except the $Zr(Fe,Cr,Nb)_2$ with hexagonal or cubic structure found only on the two alloys with the lowest Nb content. These phases likely belong to the quaternary ZrNbFeCr system, and are thought to derive from the well known $Zr(Fe,Cr)_2$ phases by small Nb addition. It is in agreement with the fact that Alloy A (see [24]) contains SPP with niobium in addition to iron and chromium, though the alloy Nb content is rather low (0.3%). These SPP should be matched with our hexagonal SPP containing large amounts of Cr and Fe and small amount of Nb found in the claddings with 0.05% Nb. Since they likely belong to the quaternary ZrNbFeCr system, we will not consider them further. If lower chromium content had been achieved, we would rather have $Zr_2(Fe,Nb)$ or $Zr_3(Fe,Nb)$.

We have also to remind that the presence of oxygen in our alloys can modify the phase domain and their stability; a study should be more specifically devoted to this topic, but we are forced now to consider that the small oxygen range (600–1200 ppm) obtained here do not cause too much variation.

The results are presented in Fig. 8, together with the data from [2] and a few unpublished data obtained by the authors. They appear very consistent together and define the domains of the ternary ZrNbFe phase diagram at 853 K. We drew the various lines to separate as reasonably as possible the alloys into binary or ternary domains as described in Section 3.2.

It exists some compositions were the αZr matrix is in equilibrium only with the hexagonal intermetallics, which was not clearly indicated in the previous diagram [2]. The hexagonal phase admits a range of composition, as will be detailed in Section 4.2, which are the extremities of the lines delimiting the binary αZr + hexagonal domain in Fig. 8.

On the very low Nb part of the diagram (Nb < 0.3 wt%), a few points seem to fall out of the corresponding domain. They correspond to the claddings with Nb < 0.3%. For the lowest, we have seen that in fact the SPP were both hexagonal and cubic, and correspond rather to $Zr(Fe,Cr)_2$ with possibly some Nb amount than to the $Zr(Nb,Fe)_2$ that are represented on the diagram. For the two other alloys (with 0.17 and 0.30 wt% Nb), the alloy exhibit hexagonal and cubic intermetallics, and in addition a few Zr_2Fe SPP. It means that the equilibrium is not reached, and we can wonder if the final equilibrium is hexagonal + cubic, or rather cubic + Zr_2Fe or Zr_3Fe. In Fig. 8 we assumed the second hypothesis and thus drew a line toward 0.2 Nb, but the first could be valid too and would lead to a limit at about 0.1 Nb. Longer annealing would be required to sort them out.

The Zr_3Fe phase has been observed by [5] in alloys with about 420 ppm iron and 0.1–0.5 wt% Nb. However, they did not find any cubic phase, and we wonder if, at least from 0.3% to 0.5% Nb, it is due to their specific heat treatment (quenching from β phase and aging).

4.2. Evolution of SPP composition with Nb and Fe in the alloy

We have seen in Fig. 2 that the composition of the hexagonal phase evolves with the niobium content. We will try below to sort the influence of the phase diagram (equilibrium composition) and the kinetics phenomena.

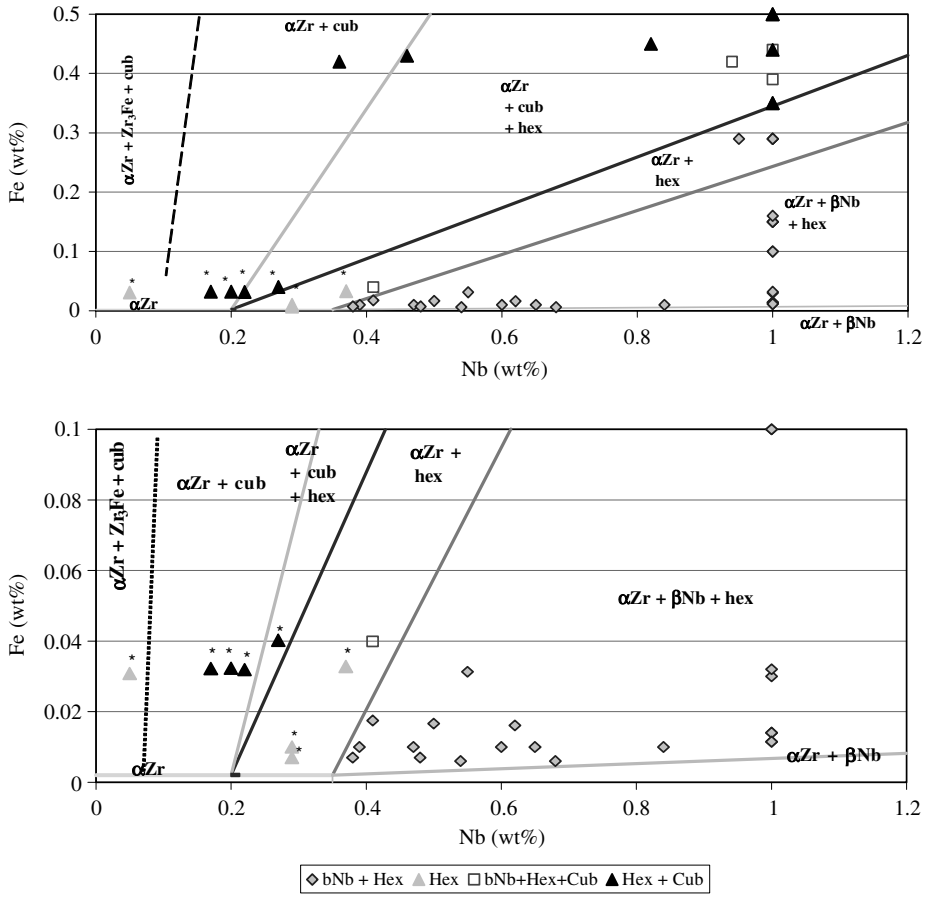

Fig. 8. Isothermal cut at 853 K of the Zr-rich corner of the Zr–Nb–Fe phase diagram. The small $*$ near some triangles indicates the presence in the corresponding sample of a non-equilibrium Zr_2Fe or $Zr(Fe,Cr)_2$-type phase.

From the phase diagram, we can derive three domains concerning the hexagonal phase. It can be in ternary domains αZr + βNb + hexagonal, αZr + hexagonal + cubic or in binary domain αZr + hexagonal. In each ternary domain, when the equilibrium is reached, the phase composition is fixed whatever the alloy composition, whereas it varies with the alloy composition according to the tie-lines in the binary one.

Here we see a clear difference between the sheets with marks 2–4 (in the αZr + βNb + hexagonal domain) and 15–17 (in the αZr + hexagonal + cubic domain). In both cases, the Nb content in the SPP is roughly independent on the Nb content in the alloy, so that we assume the equilibrium is reached; both contain no tin; the difference between the Nb content in the SPP amounts about 5 at.%, and is lower for the αZr + hexagonal + cubic domain, as could be expected from the diagram. We will thus consider that the equilibrium compositions for the hexagonal phase are (in at.%):

36 Zr 40 Nb 24 Fe for the αZr + βNb + hexagonal domain,
36 Zr 35 Nb 29 Fe for the αZr + hexagonal + cubic domain.

In the same manner, the equilibrium composition of the cubic phase in the ternary αZr + hexagonal + cubic domain could be close to:

58 Zr 11 Nb 31 Fe,

These values are in very good agreement with previous studies [2], though it is the first time that a significant existence range for the hexagonal intermetallics is reported.

However, all the hexagonal compositions do not meet these ones. For cladding with very low Nb content (Nb < 0.3%) we saw that the equilibrium was very likely not reached (existence of three SPP types instead of

two). For the other alloys, mainly sheets, the SPP composition is not very far from the two above compositions, and are mainly depleted in niobium. It means the equilibrium is not reached, due to the slow diffusion of niobium at this temperature (853 K). This holds both for hexagonal and cubic SPPs. Fig. 2 shows that the Nb content in the SPP increases with the Nb content in the alloy. Indeed, the lower the Nb content in the alloy, the lower the driving force to reach the equilibrium, and furthermore the greater the distance between SPPs.

For sheets mark 5–14 with process #2, several factors explain that the equilibrium is longer to reach compared to process #1.

1. In process #1, the hot rolling was performed in the $\alpha+\beta$ range, as for extrusion process for claddings. Thus iron and niobium segregate into the β phase; on cooling, they precipitate in a less random way (they are clustered and/or aligned), but due to smaller distances the equilibrium is reached faster.
2. The sheets transformed according to process #2 were rolled only down to 1.5 mm versus 0.4 mm for process #1, including one more cold rolling/annealing cycle. It is known that deformation can accelerate the phase transformation [25]; here we think that cold working introduces a lot of dislocations, and that the subsequent recrystallisation can accelerate the diffusion of niobium and iron through the dislocation sliding, and thus contribute to accelerate the equilibrium.
3. Last, we can assume also that tin contributes to slow down the niobium and iron diffusion, as it slows down the recrystallisation kinetics [26, p. 413], and thus reaching the equilibrium would require more time when increasing the tin content.

Further studies will be needed to know exactly what is the prominent factor.

Last, it is interesting to note that the Zr_2Fe compound has often been found when the cubic $(Zr,Nb)_4Fe_2$ intermetallics was expected. Their iron contents are roughly identical, and it can contain small niobium amounts. It is thus likely that it transforms upon further annealing into $(Zr,Nb)_4Fe_2$ by niobium incorporation.

4.3. Isothermal cut of the phase diagram at 853 K

We are thus able to propose an isothermal cut at 853 K of the Zr-rich corner of the ternary ZrNbFe phase diagram (Fig. 8). We should however remember that the equilibrium was not reached in every case, since a few metastable phases were observed in some samples and since the annealing time were rather short (a few hours); that oxygen was present in all the alloys, with variable amounts (see Table 1), which can affect the stability of some phases. Concerning this last point, we did not see in this study variations in the nature of the SPP phases, which could be correlated with variations in the oxygen content. However, this point should be confirmed by thermodynamic calculations, a first step being the modelling of this ternary diagram (without oxygen), a second one taking into account the presence of oxygen, as already done in the ZrNb(O) system [1,2]. Thus the phase diagram proposed below is, if not fully an equilibrium diagram, at least an 'industrially achievable phase diagram'.

The solubility of iron in αZr has been set to 20 wt ppm (not far from [27,28]). It is definitely less than 100 ppm. The solubility of iron in βNb has been set to 0.5 wt%, but it could be lower. The maximum niobium content in the αZr appears to be about 0.37 ± 0.05 wt% (for iron content lower than the solubility, that is 20 ppm). This precision was estimated from the available data plotted on the diagram (Fig. 8), taking into account that the points near the border lines can be on a side or the other because the equilibrium is not surely reached, and because in TEM we can observe one SPP of a type or not depending on the observed area (representativeness problem of TEM exams).

As soon as the cubic phase appears, the niobium content in the αZr matrix is lowered (at equilibrium) to about 0.1–0.2 at.%. These results are much lower than the 'classical' value of 0.6 at.%. Both [2,5] proposed values lower than 0.6 wt%, but gave no precision. It is also in agreement with the fact that Alloy A (see [24]) contains SPP with Nb though the alloy Nb content is rather low (0.3%). These SPP should be matched with the hexagonal SPP containing large amounts of Cr and Fe and small amount of Nb found in our claddings with 0.05% Nb.

4.4. SPP volume fraction

We will compute the volume fraction of SPP assuming the equilibrium: it is straightforward, knowing the chemical composition of the alloy, and the crystallographic parameters (Table 3) and composition of the phases. These values are summarised in Table 5.

The computation has been done either with the equilibrium composition of the phases, deduced from the phase diagram (Fig. 8), or from the actual composition of the phases, determined previously (Table 4). It is worth noting that a few values are missing in the column 'actual composition': for these alloys, the computation leads to negative volume fraction, which is not physical, and which arises from the non-equilibrium state of the materials.

We can see that the 2 computations, when available, are rather close to each other, and that all but 3 alloys have SPP-VF in the range 0.06–0.30%. The exceptions are the 3 alloys with high iron content (about 0.45%), and thus SPP-VF of about 2%.

Table 5
SPP volume fraction (VF) in% for the different alloys

Mark	Nb (wt%)	Fe (wt ppm)	Domain	Actual composition				Equilibrium composition			
				βNb	h	c	Total	βNb	h	c	Total
1	0.41	399	αZr + h		0.25		0.25		0.28		0.28
2	0.41	175	αZr + βNb + h	0	0.13		0.13	0	0.12		0.12
3	0.50	166	αZr + βNb + h	0.07	0.14		0.21	0.08	0.11		0.19
4	0.62	161	αZr + βNb + h	0.17	0.13		0.30	0.18	0.11		0.28
5	0.29	100	αZr + h		0.05		0.05		0.06		0.06
6	0.39	100	αZr + βNb + h	0	0.07		0.07	0	0.06		0.06
7	0.47	100	αZr + βNb + h	0.07	0.07		0.14	0.07	0.06		0.13
8	0.60	100	αZr + βNb + h	0.18	0.06		0.24	0.17	0.06		0.23
9	0.65	100	αZr + βNb + h	0.23	0.05		0.28	0.22	0.06		0.27
10	0.29	70	αZr + h		0.03		0.03		0.04		0.04
11	0.38	70	αZr + βNb + h	0	0.04		0.04	0	0.04		0.04
12	0.48	70	αZr + βNb + h	0.09	0.04		0.13	0.08	0.04		0.12
13	0.54	60	αZr + βNb + h	0.14	0.04		0.17	0.13	0.03		0.16
14	0.68	60	αZr + βNb + h	0.26	0.03		0.29	0.25	0.02		0.28
15	0.36	4200	αZr + c		0	1.98	1.98				
16	0.46	4300	αZr + h + c		0.25	1.86	2.11		0.03	2.02	2.06
17	0.82	4500	αZr + h + c		1.59	1.09	2.67		1.60	0.94	2.55
Cladd 0.05	0.05	300	?								
Cladd 0.17	0.17	300	αZr + c							0.17	0.17
Cladd 0.20	0.20	300	αZr + c							0.17	0.17
Cladd 0.22	0.22	300	αZr + h + c						0.02	0.12	0.14
Cladd 0.27	0.27	300	αZr + h		0.13		0.13		0.19		0.19
Cladd 0.37	0.37	300	αZr + h		0.16		0.16		0.21		0.21
Cladd 0.55	0.55	300	αZr + h + c	0.09	0.22		0.31	0.09	0.22		0.31

The computation was made according to the actual measured composition of the SPP or to the assumed equilibrium ones. h stands for 'hexagonal intermetallics' and c for 'cubic intermetallics'.

4.5. Corrosion/oxidation

For the corrosion/oxidation behaviour, we have to distinguish two cases:

- The low pressure tests (0.1 MPa), either in steam or in air, where no effect of Nb and Fe was observed (in the limited domains investigated); in this case, the weight gain does not seem to be sensitive to the SPP-VF, as was previously found in Zircaloy-type materials [22].
- The high pressure steam autoclave tests, where the main effect was a drastic decrease in the corrosion rate was observed with increasing the Nb content in the alloy up to 0.4 wt%, a plateau was then obtained for Nb content in the range 0.41–0.62 wt%. A secondary effect was the decrease in corrosion for a concomitant reduction of tin and increase in the iron content. In other alloys, these two elements are known to act alone in the same way as they do here. These effects are visible here whatever the temperature (688 and 773 K).

It was suggested that the main parameter acting on the corrosion behaviour of Zircaloy-type materials in high pressure steam was the SPP-VF [22]. In this study, this idea seems to hold: for each series of materials (sheets with a given process, or cladding), very high weight gains are found for the lowest Nb content, that is the lowest SPP-VF (see Table 5). However, the picture is less clear when all the data are put together, first because the SPP-VF are mainly comprised between 0% and 0.3%, that is in the low range. Only three alloys exhibits SPP-VF of about 2%; and no alloys fill the gap between 0.3% and 2%. In the lowest SPP-VF range, it was suggested that the influence of process, SPP size and distribution would be very large [22]. In our case, several different processes were used, and the SPP equilibrium composition was probably not reached in every case. This could induce also some dispersion.

The SPP-VF are thus a first order parameter under high pressure, which is more representative of PWR and BWR environments. These observations could also give some clue to the role of SPP in the oxidation/corrosion

mechanism. However, it is still not understood, and far outside the scope of this paper.

The decrease in the Nb content in solid solution in the αZr matrix was shown to lead to a improved corrosion resistance [5,29,30]. This statement is not in contradiction with what is proposed here, that is the major role of the SPP-VF. In fact, all the aforementioned studies were performed on alloys where SPP were present, likely in sufficient amount to get an overall good corrosion resistance. We can thus consider that the decrease in the Nb in solid solution is a further improvement.

5. Conclusion

Several alloys and process routes (sheets, claddings) with low niobium content, and some variations in iron and tin contents were investigated. The main following results were found:

- The Zr–Nb–Fe ternary phase diagram has been precised in the Zr-rich corner at 853 K, and the existence range of the hexagonal $Zr(Nb,Fe)_2$ compound has been obtained.
- The solubility limit of Nb in αZr appears equal to 0.37 ± 0.05 wt%, while the niobium content in αZr decreases to about 0.1–0.2 wt% when the cubic $(Zr,Nb)_4Fe_2$ phase appears.
- Up to 1% Sn, there is no influence of tin on the SPP nature and composition; but tin degrades the corrosion resistance in autoclave at 773 and 688 K.
- The equilibrium composition is longer to reach for dilute alloys.
- Last, the steam corrosion behaviours show a very great dependence on the exact process for the lowest SPP-VF, and very high weight gain can be obtained. The air oxidation is much less affected by this parameter.

Longer annealing treatments are needed to reach the equilibrium, and the Zr–Nb–Fe ternary phase diagram should still be precised in the region between the cubic $(Zr,Nb)_4Fe_2$, the Zr_3Fe and Zr_2Fe regions, as regards the existence range of these compounds, particularly their niobium solubility limit. It would also be interesting for the in-reactor behaviour to derive the equilibrium diagram at lower temperatures, representative of the operating temperatures.

Acknowledgements

We would like to thank C. Toffolon-Masclet and J.C. Brachet (CEA-Saclay, SRMA) for interesting discussions.

References

[1] C. Toffolon, PhD thesis, CEA-R-5917 (2000).
[2] C. Toffolon-Masclet, J.C. Brachet, C. Servant, L. Legras, D. Charquet, P. Barberis, J.P. Mardon, Zirconium in the Nuclear Industry: Thirteenth International Symposium, ASTM STP 1423, 2002, p. 361.
[3] M.S. Granovsky, M. Canay, E. Lena, D. Arias, J. Nucl. Mater. 302 (2002) 1.
[4] M. Canay, C.A. Danon, D. Arias, J. Nucl. Mater. 280 (3) (2000) 365.
[5] Y.H. Jeong, H.G. Kim, T.H. Kim, J. Nucl. Mater. 317 (1) (2003) 1.
[6] J.P. Mardon, D. Charquet, J. Senevat, International Topical Meeting on Light Water Reactor Fuel Performance (1994) Proceedings, p. 643.
[7] J.P. Mardon, G. Garner, P. Beslu, D. Charquet, J. Senevat, ANS International Topical Meeting on Light Water Reactor Fuel Performance, Portland (Oregon), 2–6 March 1997, p. 405.
[8] J.P. Mardon, D. Charquet, J. Senevat, ASTM STP 1354 (2000) 505.
[9] A.V. Nikulina, J. Nucl. Mater. 238 (1996) 205.
[10] V.N. Shishov, A.E. Nikulina, V.A. Markelov, M.M. Peregud, A.V. Kozlov, S.A. Averin, S.A. Kolbenkov, A.E. Novoselov, Zirconium in the Nuclear Industry: Eleventh International Symposium, ASTM STP 1295, 1996, p. 603.
[11] V.N. Shishov, M.M. Peregud, A.E. Nikulina, S.N. Akhromov, A.E. Novoselov, G.P. Kobylyansky, Z.E. Ostrovsky, V.K. Shamardin, Zirconium in the Nuclear Industry: Thirteenth International Symposium, ASTM STP 1423, 2002, p. 758.
[12] R. Kapoor, S.L. Wadekar, J.K. Chakravartty, Mater. Sci. Eng. A: Struct. Mater. 328 (1–2) (2002) 324.
[13] Y. Kim, S. Kim, J. Nucl. Mater. 270 (1–2) (1999) 147.
[14] T.R.G. Kutty, T. Jarvis, C. Ganguly, J. Nucl. Mater. 246 (2–3) (1997) 189.
[15] P. Mukherjee, P.M.G. Nambissan, P. Sen, P. Barat, S.K. Bandyopadhyay, J. Nucl. Mater. 273 (1999) 338.
[16] P. Mukherjee, P. Barat, S.K. Bandyopadhyay, P. Sen, S.K. Chattopadhyay, S.K. Chatterjee, A.K. Meikap, M.K. Mitra, Metall. Mater. Trans. A 31 (10) (2000) 2405.
[17] J.A. Sawicki, J. Nucl. Mater. 264 (1999) 169.
[18] M.P. Van Effenterre, PhD thesis, 1972.
[19] P. Bossis, PhD thesis, 1999.
[20] P. Bossis, F. Lefebvre, P. Barberis, A. Galerie, Mater. Sci. forum (2001) 255.
[21] M. Tupin, PhD thesis, Ecole Nationale Supérieure des Mines de Saint Etienne, France, 15-10-2002.
[22] P. Barberis, E. Ahlberg, N. Simic, D. Charquet, C. Lemaignan, G. Wikmark, M Dahlbäck, M Limbäck, P. Tägtström, B. Lehtinen. Thirteenth International Symposium on Zirconium in the Nuclear Industry, ASTM STP 1423, 2002, p. 33.
[23] M. Tupin, M. Pijolat, F. Valdivieso, M. Soustelle, A. Frichet, P. Barberis, J. Nucl. Mater. 317 (2–3) (2003) 130.
[24] A.M. Garde, G.P. Smith, R.C. Pirek, M Dahlbäck, L. Hallstadius, Zirconium in the Nuclear Industry: 13th International Symposium, ASTM STP 1423, 2002, p. 490.

[25] J.D. Embury, A. Deschamps, Y. Brechet, Scr. Mater. 49 (2003) 927.
[26] B. Lustman, F. Kerze Jr., Metallurgy of Zirconium, McGraw Hill Book Company, New York, 1955.
[27] R. Borrelly, P. Merle, L. Adami, J. Nucl. Mater. 170 (1990) 147.
[28] H. Zou, G.M. Hood, J.A. Roy, R.J. Schultz, J.A. Jackman, J. Nucl. Mater. 210 (1994) 239.
[29] K.N. Choo, Y.H. Kang, S.I. Pyun, V.F. Urbanic, J. Nucl. Mater. 209 (1994) 226.
[30] Y.H. Jeong, K.O. Lee, H.G. Kim, J. Nucl. Mater. 302 (1) (2002) 9.